ADVANCED FUNCTIONAL MATERIALS
www.afm-journal.de

Zero-Frequency Bandgap Metamaterials: The Mosaic Design Strategy

*Nan Gao, Vicente Romero-García, Jean-Philippe Groby, and Ping Sheng**

Bandgaps constitute the central feature of photonic and phononic crystals. However, the zero-frequency bandgap, defined here as the absence of wave states from 0+ to a finite frequency, is generally regarded as not realizable for the Bragg mechanism since the lattice constants need to be very large to infinite. Moreover, a structure or material that displays a zero-frequency bandgap would present a challenge to the theory of homogenization, which is predicated on the existence of low-frequency, long-wavelength excitations, for which the effective material parameters apply. In this work, the finite-sized tiles are utilized, linked together at their corners, to create a mosaic plate system that can display static rigidity with translational degrees of freedom. Full waveform simulation results on the mosaic plate show a clear zero-frequency bandgap, which are verified experimentally by laser vibrometer scanning of modes excited by a harmonic point source, as well as by comparison of sound transmission loss (TL) between the mosaic plate and a uniform plate with similar mass density. The latter comparison shows the mosaic plate to have a 13 dB advantage in TL at 50 Hz, and deviates from the mass density law over a broad low-frequency range.

1. Introduction

In thin infinite plates, low-order antisymmetric bending modes dominate elastic wave propagation and are critical for acoustic device design.[1] Bending waves are characterized by out-of-plane displacement, and they are particularly important for the design of acoustic and elastic wave devices in plate configurations. However, suppressing low-frequency bending waves, especially starting from zero frequency, can pose a significant challenge. Phononic crystals (PnCs) with the bandgap effect have provided an approach for attenuating elastic bending waves.[2–14] Conventional approaches (e.g., applying zero displacement constraints to PnCs,[15] either directly or indirectly,[16–18] or Bragg-scattering-based PnCs) often impose impractical translational rigidity or require bulky periodic structures. Since zero displacement constraints imply the loss of translational degrees of freedom, such systems would be difficult to transport.

Alternative strategies like quasi-zero-stiffness designs,[19–22] inertial amplification,[23–25] geometric nonlinearity,[26,27] and the combination of the above mechanisms[28] can address low-frequency bandgaps without relying solely on Bragg mechanisms. Recent research on curved and hierarchical metamaterials has explored alternative mechanisms for wave manipulation. Curved configurations[29–32] leverage geometric curvature to steer wave propagation, reduce effective stiffness, and induce mode localization, thereby achieving subwavelength attenuation and low-frequency vibration control. Hierarchical architectures,[33–35] on the other hand, broaden bandgaps through coupled multiscale resonances. However, both approaches face inherent limitations: neither supports zero-frequency bandgaps, and their low-frequency performance remains within a narrow frequency range. Curved metamaterials are sensitive to geometric imperfections, while hierarchical designs suffer from inter-scale energy leakage that weakens bandgap effectiveness. Moreover, quasi-zero-stiffness systems utilize nonlinear geometric effects to create high-static-low-dynamic stiffness regions, enabling low-frequency vibration isolation. However, the narrow operational bandwidth (in the range of several to a few tens of Hz) limits their practical utility. Inertial amplification achieves low-frequency bandgaps by enhancing local inertia through weak mechanical linkages, but it often leads to narrow bandwidths, increased structural complexity, and reduced robustness. These trade-offs between bandwidth, complexity, and scalability reflect the broader challenge of balancing lightweight design with broadband performance across various acoustic and mechanical applications. These challenges are

N. Gao, V. Romero-García
Instituto Universitario de Matemática Pura y Aplicada
Departamento de Matemática Aplicada
Universitat Politècnica de València
Camino de Vera, València 46022, Spain

J.-P. Groby
Laboratoire d'Acoustique de l'Université du Mans (LAUM)
UMR 6613, Institut d'Acoustique - Graduate School (IA-GS)
CNRS Le Mans Université
Avenue Olivier Messiaen, Le Mans 72085 Cedex 09, France

P. Sheng
The Hong Kong University of Science and Technology
Hong Kong, China
E-mail: sheng@ust.hk

P. Sheng
Associate of Clare Hall College
Cambridge University
Cambridge CB3 9AL, UK

The ORCID identification number(s) for the author(s) of this article can be found under https://doi.org/10.1002/adfm.202508243

DOI: 10.1002/adfm.202508243

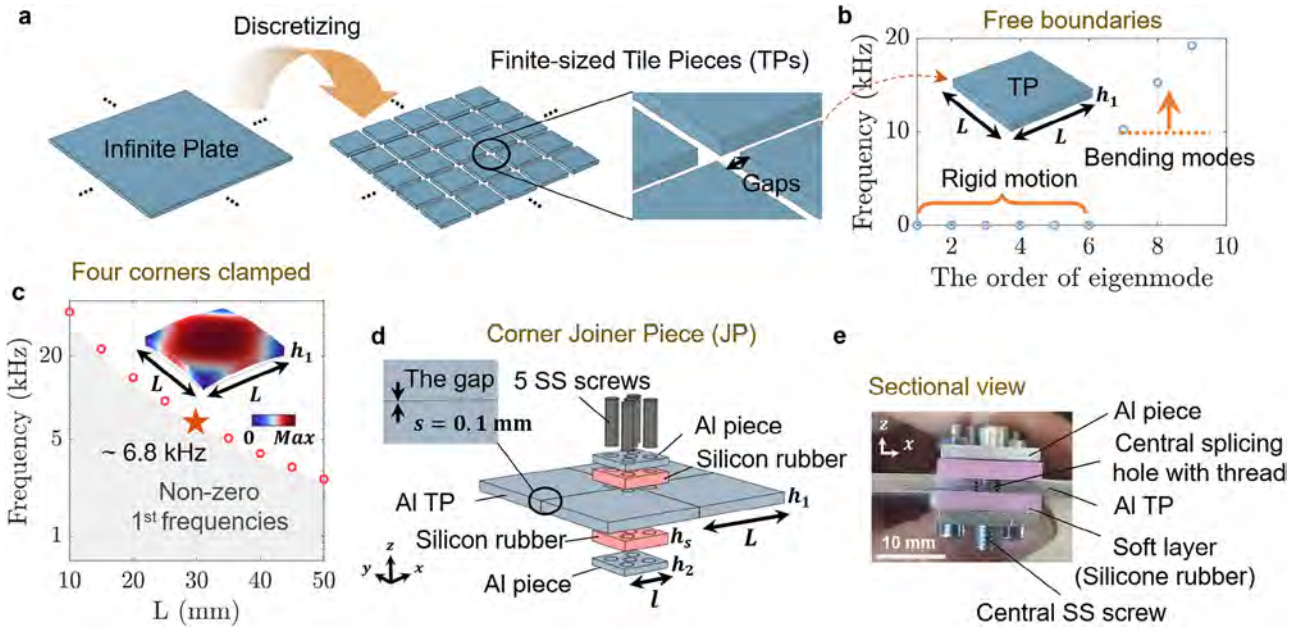

Figure 1. Mosaic design strategy: a) A thin plate is divided into countless small finite-sized tile pieces (TPs), leaving 0.1 mm gaps between them. b) The first 10 eigenfrequencies for a TP with free boundaries ($h_1 = 3$ mm, $L = 30$ mm), where the first 6 are rigid body motions. The discrete eigenmodes starting with the 7th are the locally resonant modes with free boundary conditions. c) For a TP with a thickness of 3 mm and four corners clamped, its first-order bending mode frequency is plotted as a function of the in-plane size (L) of the TP. The frequency for the size used in the present experiments ($L = 30$ mm), 6.8 kHz, is marked by a red star. d) Illustration of the corner joiner piece (JP) with screws. A JP comprises alternating hard and soft layers set at the four corners of each TP. Every JP has two aluminum alloy pieces, each with side length $l = 15$ mm, thickness $h_2 = 2$ mm. Two silicone rubber layers with side length $l = 15$ mm thickness and $h_s = 3$ mm, are sandwiched symmetrically between the TP and the aluminum pieces. The whole assembly is tightly connected by five stainless steel screws. The central screw, 4 mm in diameter, runs through each of the four TPs' corners. The other four screws are 3 mm in diameter. e) A photo of the JP and its components.

particularly acute in architectural acoustics, where real-world building components demand simultaneous thin profiles and broadband insulation against urban traffic noise—requirements unmet by current quasi-static or narrowband solutions.[36,37]

To overcome the aforementioned challenges, we propose a mosaic design strategy to achieve a broadband zero-frequency bandgap in flexural modes of a structured plate. It is well known that a finite-sized solid plate has a finite eigenfrequency above zero, whose value depends on the applied boundary conditions on the plate's edges and its material properties. Since the term zero frequency bandgap applies only to infinite samples, we must therefore link the finite-sized pieces to form a large, if not infinite, plate. These finite-sized pieces are denoted tile pieces (TPs), and the final structure formed by connecting them is denoted a mosaic plate (MPt). Can such a "restored" infinite MPt still preserve the finite eigenfrequency character of the small constituent TPs, displaying locally resonant modes, while being a connected part of the whole structure? Clearly, most schemes of linking the small TPs together would restore a homogenized plate's low-frequency bending wave behavior. To achieve the goal of a viable zero-frequency bandgap plate, it is necessary to disable the low-frequency bending wave excitations in the linked system. Here we propose a scheme that uses multilayered corner joints, to connect square-shaped aluminum TPs, to attain the desired effect.

2. Results and Discussions

2.1. Mosaic Design Strategy

Shown in **Figure** 1a is a homogeneous plate discretized into numerous finite-sized TPs, with gaps left between adjacent pieces. The eigenfrequencies of a TP with free boundaries, 3 mm in thickness and 30 mm × 30 mm in lateral dimensions, are shown in Figure 1b. The six degenerate zero-frequency eigenmodes correspond to the rigid-body motions of the TP. Finite frequency bending modes appear beyond these six degenerate zero modes; the eigenfrequencies of these modes are determined by the material parameter (bending stiffness) as well as the geometric dimension of the TP. As shown in Figure 1c, the lowest eigenfrequency of the bending mode increases significantly as the side length decreases. To eliminate the influence of rigid body motion, the TP is clamped at its four corners in this case.

Based on the above, obtaining a broadband zero-frequency bandgap requires the following two conditions:

1) Separation and decoupling: the discrete plate units must remain separated to ensure flexural decoupling, which allows each TP's bending mode to be that of the entire structure's minimum bending mode frequency, thereby defining the upper limit of the bandgap; and 2) Rigid joint: a certain degree of rigid constraints must be applied to the corners of TPs, intended to not only suppress the bending wave propagation from one TP to its

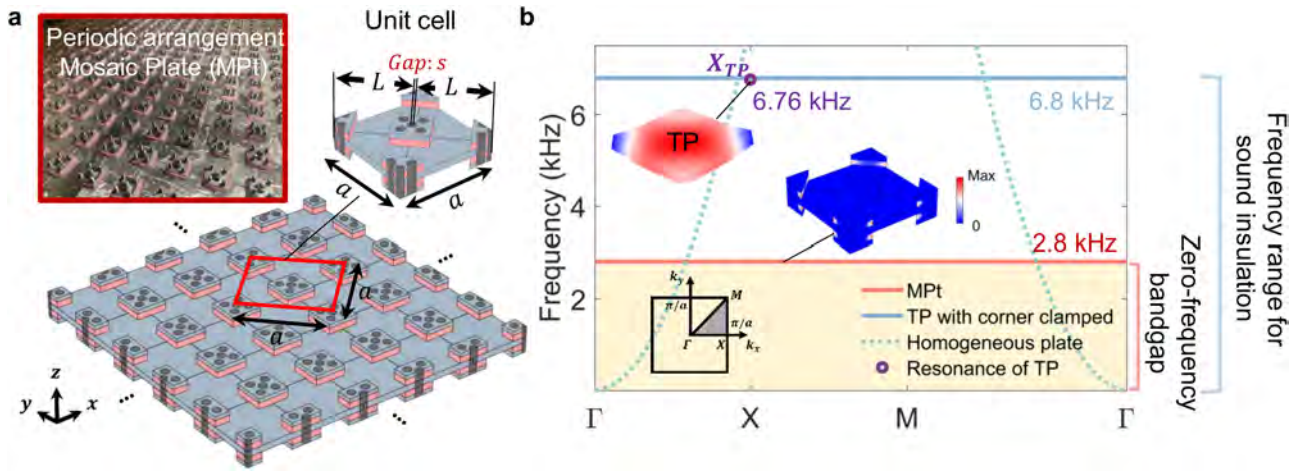

Figure 2. Structure of the mosaic plate and the zero-frequency bandgap by simulations: a) Schematic diagram of the MPt and the unit cell, delineated by the red dashed line, used in the simulations with the Bloch-Floquet boundary condition. Upper left inset: A photo of the actual sample. Upper right inset: The simulation unit cell with its dimensions delineated. Here the lattice constant $a = \sqrt{2}\,(L + s)$. b) Simulated dispersion relation of the MPt. The flat dispersion, delineated by the red line, indicates localized soft layer modes at 2.8 kHz. These modes are marked by the bright spots in the inset to the upper right. The localized mode at 6.8 kHz, delineated by the flat blue line, is that of a single TP with four corners clamped. The locally resonant mode at 6.76 kHz at the X point, denoted X_{TP}, is marked by a colored circle. The green dotted line is the bending mode dispersion relation of a homogeneous aluminum plate with a thickness of 3 mm. Upper right inset: Displacement magnitude of the unit cell at 2.8 kHz, with the bright spots marking the soft layer resonances. Upper left inset: The locally resonant mode at the X point. Similarity is noted to the isolated TP resonance with four corners fixed (Figure 1c). Asymmetry between the two diagonals of the X_{TP} mode is due to the symmetry of the mode at the X point. Lower left inset: The irreducible Brillouin zone of a square lattice is used to plot the results of the simulations. The yellow-shaded region indicates the zero-frequency bandgap. Since the localized soft layer resonance is not coupled to the incident sound, the sound insulation can be extended to 6.8 kHz.

neighbors, but also to provide structural support for the overall system. By fulfilling these two conditions, the design ensures both structural stability and facilitates the creation of a broadband zero-frequency bandgap.

In Figure 1d, we illustrate the rigid corner connection of the TPs to form the MPt. Each TP, made of aluminum alloy with Young's modulus $E = 69$ GPa, density $\rho = 2700\ \mathrm{kg\ m^{-3}}$, and Poisson ratio $\nu = 0.33$, is linked at each corner to its neighbors by a 4 mm diameter stainless steel screw, with $E = 219$ GPa, $\rho = 7903\ \mathrm{kg\ m^{-3}}$, and $\nu = 0.32$. However, since the screw can tilt slightly to result in second-order lateral displacements that can destabilize the structure, we use an aluminum alloy joiner piece (JP) to counter such effect. Each JP comprises two aluminum (Al) plates, each 15 mm by 15 mm and 2 mm in thickness, with four additional screws (each 3 mm in diameter), together with two soft silicone rubber layers, each 15 mm by 15 mm and 3 mm in thickness, that are sandwiched between the two Al plates and the TP in the middle. The whole corner connection structure, symmetrical with respect to the central TP, is illustrated in Figure 1d, with a photo of the actual composite JP unit shown in Figure 1e. The functions of the soft layers are threefold. First, they provide shear resistance to any collective second-order lateral displacement of the screws. Second, they also shield the force/torque resulting from the bending displacement of each TP from being transmitted to its neighbors through the JPs. Third, the soft layers provide a damping effect on TPs' normal displacements by converting them to lateral displacements of the soft layers at the open boundaries. This effect is particularly important in giving the MPt an advantage over the mass density law in attenuating sound transmission.

It is to be noted that the quarter of the hole for the central screws, on each corner of TP, is threaded (Figure 1e) so as to ensure that the central screw tightly connects the four neighboring TPs. The combination of the silicone rubber layer and the pretightening force of the bolts introduces damping to the system but also improves the overall rigidity of the structure. This junction design effectively balances decoupling and static rigidity, enabling the mosaic plate system to attain both structural support while maintaining the vibrational isolation of each TP.

Additionally, the whole structure offers excellent lightweight and scalable manufacturability by using standard aluminum components and readily available fasteners without the need for specialized materials or metal 3D printing. Soft silicone layers can be rapidly reproduced using reusable molds, enabling efficient and low-cost mass production. (Refer to Section S1, Supporting Information, for details of the sample production and assembly)

2.2. Zero-Frequency Bandgap Effect

By applying the above joint design to the corners of each TP and arranging them periodically, the final MPt can be obtained as shown in **Figure 2a**. The portion enclosed by the red dashed line is selected as the unit cell of this periodic structure, with the Bloch-Floquet boundary conditions applied to its boundaries for simulations. The wave vector k was swept along the boundary of the irreducible Brillouin zone for a square lattice (shadow region in the inset of Figure 2b), to numerically solve the eigenvalue problem $\omega(k)$. The first-order dispersion curve (red line

in Figure 2b) reveals a zero-frequency bandgap spanning 0+ to 2.8 kHz (indicated by the yellow-shaded region); there are no propagation modes within the bandgap range. Apart from the degenerate rigid motion mode at zero frequency, the mode of the flat band at 2.8 kHz corresponds to the resonance mode of the soft layer. This vibration mode exhibits predominantly in-plane deformation, indicated by the bright spots shown in the inset of Figure 2b. Owing to their very small footprints, the localized soft layer modes can only have minimal coupling with sound waves incident on the MPt. Hence the upper limit of the sound insulation frequency, defined by the normal displacements of the MPt, is determined by the locally resonant mode of the TP, approximated by the lowest-order mode at 6.8 kHz as shown in Figure 1c. We have also identified such a locally resonant mode in the simulations on the MPt, shown in Figure 2b, with an eigenfrequency of 6.76 kHz at the X point. This is very close to the TP resonance with corners clamped. The displacement profile of the locally resonant mode at X_{TP} is also similar to that of the isolated TP resonance shown in Figure 1c, with the exception of the asymmetry between the two diagonals, as dictated by the symmetry of the X point. The TP resonances at the M and Γ points, with frequencies of 6.799 and 6.798 kHz, respectively, are highly hybridized with the near-continuum of soft layer and other modes. They exhibit a much less distinct localized displacement profile than that at the X point (see Section S6, Supporting Information for details). Hence, 6.8 kHz may be regarded as the demarcation frequency above which the global excitations begin to appear. These results indicate that the upper edge frequency of the band gap in the mosaic plate originates from the local resonance of a single tile with four corners fixed. Since this local resonance frequency can be tuned by varying the lateral size of the tile, as shown in Figure 1c, it follows that the size of the zero-frequency bandgap can be tuned by scaling the size of the tile.

While the upper edge of the band gap in the mosaic plate structure still originates from the local resonance of the tiles. It differs significantly from the conventional locally resonant metamaterials. The main function of the mosaic structure lies in the effective low-frequency decoupling between units, which can suppress global bending modes at low frequencies. However, individual tiles' bending modes can exist at higher frequencies.

It is also worth noting that the starting frequency of the zero-frequency bandgap is 0+, which suggests that the mosaic plate can undergo rigid-body displacement as a whole. This feature frees the design from the requirement of being fixed to the ground, offering greater flexibility for practical applications. In this context, 0 Hz can also be regarded as the first resonance of the mosaic plate, and thus, the mechanism of the zero-frequency band gap can be interpreted using the Green function.

2.3. Green Function and Point-Excitation Vibration Experiment

2.3.1. Green Function for Zero-Frequency Bandgap System

The elastic deformation response of a solid under a point source pressure can be given by the Green function, which represents the ratio between the deformation displacement ξ at position x and a source pressure p at x', with angular frequency:

$$G(x,x',\omega)=\frac{\xi}{p}=\sum_{n=1}^{N}\frac{\phi_n^*(x)\phi_n(x')}{m_n(\omega_n^2-\omega^2-i\beta_n\omega)}. \tag{1}$$

Here ϕ is the *n-th* eigenfunction in the unit of displacement, $\omega_n = 2\pi f_n$ is the associated angular eigenfrequency, $\omega = 2\pi f$ is the angular frequency of the source, and β_n is the dissipation coefficient of the system associated with the nth eigenfunction. Hence, the displacement at x can be expressed as

$$\xi(x,x',\omega)=p\sum_{n=1}^{N}\frac{\phi_n^*(x)\phi_n(x')}{m_n(\omega_n^2-\omega^2-i\beta_n\omega)}. \tag{2}$$

In the case of a zero-frequency bandgap, there are no eigenfunctions between the lower bandedge and the upper bandedge. In the intermediate frequency range, the displacement field of the solid is given by

$$\xi(x,x',\omega)\cong\frac{\phi_0^*(x)\phi_0(x')p}{m_0(\omega_0^2-\omega^2-i\beta_0\omega)}+\frac{\phi_1^*(x)\phi_1(x')p}{m_1(\omega_1^2-\omega^2-i\beta_1\omega)}+\frac{\phi_2^*(x)\phi_2(x')p}{m_2(\omega_2^2-\omega^2-i\beta_2\omega)}. \tag{3}$$

It should be noted from Equation (3) that the absence of modes in the bandgap frequency range does not imply zero response in the relevant frequencies. Here the zeroth order eigenfunction is that of the rigid body motions, the first order eigenfunction is the one with eigenfrequency at $f_1 = 2.8$ kHz, while the second order eigenfunction is that with eigenfrequency at $f_2 = 6.8$ kHz, the locally resonant mode. It is noted that the first-order eigenfunction has a limited spatial extent since it is localized in the soft layer, hence its contribution to the overall displacement is negligible.

Here we would like to note that regarding the earlier remark concerning the challenge to the homogenization theory, the Green function approach can give a more general overview of this comment. In the absence of low-frequency excitation modes, the Green function still provides the response function to a point excitation. The Green function approach can be reduced to the effective medium theory when the self-energy term arising from multiple scatterings, in the low frequency range, is wave vector k-independent. However, in the present case, the response to the point excitation is clearly tied to the position of the excitation and the distance from it. That implies k dependence on the self-energy.[38] Hence, any new approach to the homogenization theory for our present system must take that into account.

2.3.2. Vibration Transmission Verification

As is well known, the Green function is the solution of a linear differential equation under a point-source excitation (i.e., a Dirac delta function). According to the principle of superposition, the response to an arbitrary excitation can be expressed as the convolution integral of the Green function with the excitation function. This approach is widely used across physics and engineering. Based on the Green function interpretation of the

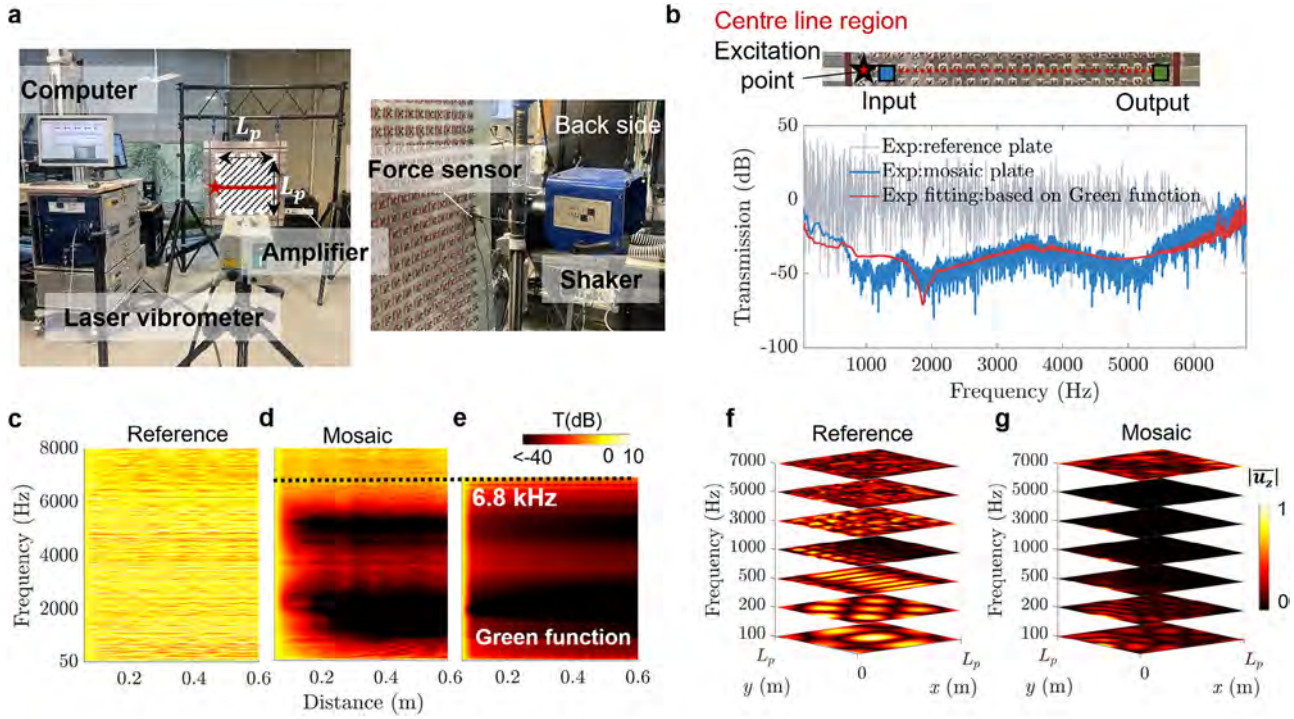

Figure 3. Vibration transmission test for the mosaic plate and the reference plate: a) Photos of the setup for the vibration test, where the laser vibrometer scanning area is delineated with side length L_p (20×20 TPs). Details of the experimental setup can be found in Section S3 (Supporting Information). b) Upper panel: Centre line region of the MPt (red dash line in (a)) for evaluating the vibration signal transmitted from the source to the measurement point, 0.6 m away. The red star indicates the excitation position of the shaker, and the red dashed line is the central line for measuring the transmitted signal at various distances from the source, shown in (c–e). The blue and green squares indicate the pickup area for the input and output signals, respectively. Lower panel: Experimental results of mosaic plate's transmission (blue line) as a function of frequency, compared with the fitting result based on the Green function (red line). The transmission of a 2 mm stainless steel reference plate with the same mass and lateral dimensions is shown by the gray line. While the MPt transmission results show significant decay, the same results for the reference plate show no significant decay, apart from large fluctuations arising from the discreteness of the excitation modes due to sample's finite size. c) Vibration transmission as evaluated from Equation (4) for the reference plate, plotted as a function of distance away from the source. The frequency covered is from 50 Hz to 8 kHz. d) The same for the MPt, where the black dash line represents the upper edge of the bandgap at 6.8 kHz. e) Fitting results based on the Green function, where the color represents transmission in dB. f,g) The comparison of experimental displacement velocity fields of the reference plate and MPt over the cross-sectional area of the sample, at selected frequencies (100 Hz, 200 Hz, 500 Hz, 1 kHz, 3 kHz, 5 kHz and 7 kHz). Here the color represents the value of normalized out-of-plane displacement velocity; white denotes 1 and black means zero.

zero-frequency band gap presented in the previous section, we further validate the mechanism by vibration transmission experiment with a point excitation to the MPt.

Here, we performed vibration transmission tests on the MPt, as well as on a 2 mm thick stainless-steel plate of the same mass and in-plane dimensions for comparison. For this experiment, we used a point harmonic source excited by a shaker (The Modal Shop 2075E), and a laser vibrometer measurement system, as shown in **Figure 3**a. The sample was suspended at its four corners using two types of cords (non-elastic and elastic) attached to a rigid frame, while the remaining boundaries were left free. (Refer to Section S3, Supporting Information, for details of the experimental setting) The scanning area for the laser vibrometer (Polytec PSV-500) is $L_p \times L_p \cong 0.6\ \text{m} \times 0.6\ \text{m}$ (shaded region in Figure 3a). The averaged out-of-plane velocity within the blue region at the beginning of the centerline (see upper panel of Figure 3b) was selected as the input signal v_{input}; while the green region at the end of the centerline (see upper panel of Figure 3b) was chosen as the output region. The average out-of-plane displacement velocity is denoted v_{output}. The transmission signal of the sample is defined by

$$T = 20\log\left(\frac{\left|v_{\text{output}}\right|}{\left|v_{\text{input}}\right|}\right)(dB). \tag{4}$$

In the experiment, we only measured the amplitude of the out-of-plane displacement velocity. Hence for the ease of comparison Equation (3) is rewritten as:

$$\begin{aligned}\left|v(x,x',\omega)\right| &\cong \left|\frac{\phi_0^*(x)\phi_0(x')p\omega}{m_0(\omega_0^2-\omega^2-i\beta_0\omega)}+\frac{\phi_1^*(x)\phi_1(x')p\omega}{m_1(\omega_1^2-\omega^2-i\beta_1\omega)}+\frac{\phi_2^*(x)\phi_2(x')p\omega}{m_2(\omega_2^2-\omega^2-i\beta_2\omega)}\right| \\ &\cong \left|\frac{\gamma_0\omega}{\omega_0^2-\omega^2-i\beta_0\omega}+\frac{\gamma_1\omega}{\omega_1^2-\omega^2-i\beta_1\omega}+\frac{\gamma_2\omega}{\omega_2^2-\omega^2-i\beta_2\omega}\right|\cdot\sqrt{\frac{a}{|x-x'|}},\end{aligned} \tag{5}$$

where $f_0 = 0$, $f_1 = 2.8$ kHz, and $f_2 = 6.8$ kHz represent the three eigenfrequencies between the lower and upper boundaries of the bandgap; γ_0, γ_1, and γ_2 are parameters related to m_0, m_1 and m_2;

$\sqrt{\frac{a}{|x-x'|}}$ is the distance factor that accounts for the spreading of a point source in two dimensions, and a is the lattice constant. Since the localized resonance modes of the soft layer are primarily confined to in-plane motion, their influence can be neglected, i.e., $\gamma_1 = 0$ is used for simplification. By substituting the experimental input data at the source point, the vibration transmission based on the Green function can be expressed as

$$T = 20\log\left(\frac{\left|v(x,x',\omega)\right|}{\left|v_{input}\right|}\cdot e^{-Cf}\right)(dB), \tag{6}$$

where C is the dissipation coefficient caused by the soft layers. We used the least squares method to fit the parameters $b = [\gamma_2, \beta_0, \beta_2, C]$ in the Green function expression, by using the experimental data:

$$\min_b \left\| T(\omega,b) - T^{\exp}\right\|_2^2 = \min_b \sum_{i=1}^{N}\left(T(\omega_i,b) - T_i^{\exp}\right)^2, \tag{7}$$

where $T(\omega, b)$ is the fitting result (Equation 6), and T^{exp} denotes the experimental results, evaluated by using Equation (4). The final optimal parameter combination can be obtained as $\gamma_0 = 1.07\ \mathrm{m\,s^{-2}}$, $\gamma_2 = 13.28\ \mathrm{m\,s^{-2}}$, $\beta_0 = 170.55$ Hz, $\beta_2 = 1021.08$ Hz, $C = 5.05\times10^{-4}$ s (Refer to Section S2, Supporting Information for details of the least squares fitting and parameter analysis).

Shown in Figure 3b are the experimental results, measured as a function of frequency, for the MPt and the reference plate, as well as the fitting results based on the Green function. The comparison reveals that the MPt exhibits a significant reduction in vibration transmission between the source and the measurement point 0.6 m away. Between 50 Hz (the lowest measured frequency) and 6.8 kHz, the measured vibration transmission trend aligns closely with that predicted by the Green function fitting results. In comparison, for the reference plate, the out-of-plane displacement velocity fields at the measurement point display a flat (average) center line with large fluctuations as a function of frequency, owing to the discreteness of modes in the finite-sized sample. In Figure 3c,b,e, we show the data for the transmitted signals at different distances from the source: 3c the reference plate, 3d the MPt, and 3e the Green function prediction. It is observed that the transmitted signal of the reference plate does not show any sign of decay as a function of distance, whereas for the MPt the signal decay is obvious. This decay is reproduced by the Green function prediction as a function of distance away from the source. Figure 3f,g shows the cross-sectional excitation profiles for the reference plate and the MPt at different frequencies. Locally resonant modes in the MPt appear only at around 6.8 kHz. Owing to the influence of the boundaries of the finite structure, wave propagation still occurs at low frequencies (less than 100 Hz) in the experiment, which is an unavoidable experimental limitation. In conclusion, it is evident that the upper limit of the bandgap, as presented by the transmission spectrum, closely matches the first bending mode frequency of a single TP with four corners clamped at 6.8 kHz. Additionally, near the middle of the bandgap, a slight increase in transmission is observed in Figure 3b. This is attributed to the addition of the two Lorentzian tails from the zeroth order mode and the second order mode.

2.4. Sound Transmission

Sound attenuation through reflection, especially in the low-frequency regime, has always been an important topic for the envisioned use of zero-frequency bandgap materials as the reflecting wall. The absence of low-frequency modes is expected to decouple the incident sound from the wall. According to the mass density law,[39] increasing the areal mass density of a wall can significantly enhance its sound insulation capability, especially in the low-frequency range. However, for many applications, strict weight and space limitations can mean the impracticality of increasing the thickness or density to improve sound insulation performance. Due to the absence of excitable modes in the zero-frequency bandgap range, the MPt is an ideal material system to overcome the limitations imposed by the mass density law in the low-frequency range.

The experimental setup for the sound insulation test consists of two chambers: a reverberation chamber as the source room, and a semi-anechoic chamber on the receiver side (**Figure** 4a), separated by a window in which the sample is to be firmly anchored. The sample was clamped by two wooden frames and fixed to the wall that defines the edge of the window (Figure 4b). Because of the 0.1 mm gaps between the TPs, sound leakage from these gaps could impact the sound insulation performance. Here, we applied engine oil to the gaps, which has a large impedance mismatch with air (illustrated in Figure 4c) to mitigate the sound leaking effect. Engine oil can adhere to the metal surface to form a stable thin film. During the test, the source room emits sound signals from two corner speakers. The diffuse incident sound waves reaching the sample window, p_{in}, were represented by the captured sound from a microphone array placed in the center region of the source room. A sound intensity probe (B&K Type 3599) was used in the receiving room to scan the sound field near the surface of the sample, to obtain the averaged value p_{out} across the sample surface area. The acoustic transmission loss of the sample is expressed as

$$TL = 20\log\left(\frac{\left|p_{in}\right|}{\left|p_{out}\right|}\right)(dB). \tag{8}$$

The experiment and simulation results on the MPt are shown in Figure 4d as red line and blue circles, respectively. The same test was carried out on the reference plate for comparison; the results are plotted in Figure 4d as the yellow line. The mass density law is shown as the green dashed line. We observe that the transmission loss (TL) of the mosaic plate remains relatively flat at low frequencies (below 1 kHz), with an average TL of 30 dB (experiment) and 35 dB (simulation). In the mid to high-frequency range, the trend tends to align with the mass density law, but the TL is consistently 5 dB higher than that predicted by the mass density law. A significant change in the simulation results is seen near the upper edge of the bandgap (6.8 kHz), where local resonance occurs, so a sharp increase in transmission (i.e., a decrease in TL) is seen. For the reference plate, its trend in low frequencies is consistent with the mass density law. However, due to the diffuse sound incidence in the experiment, the trend deviates from

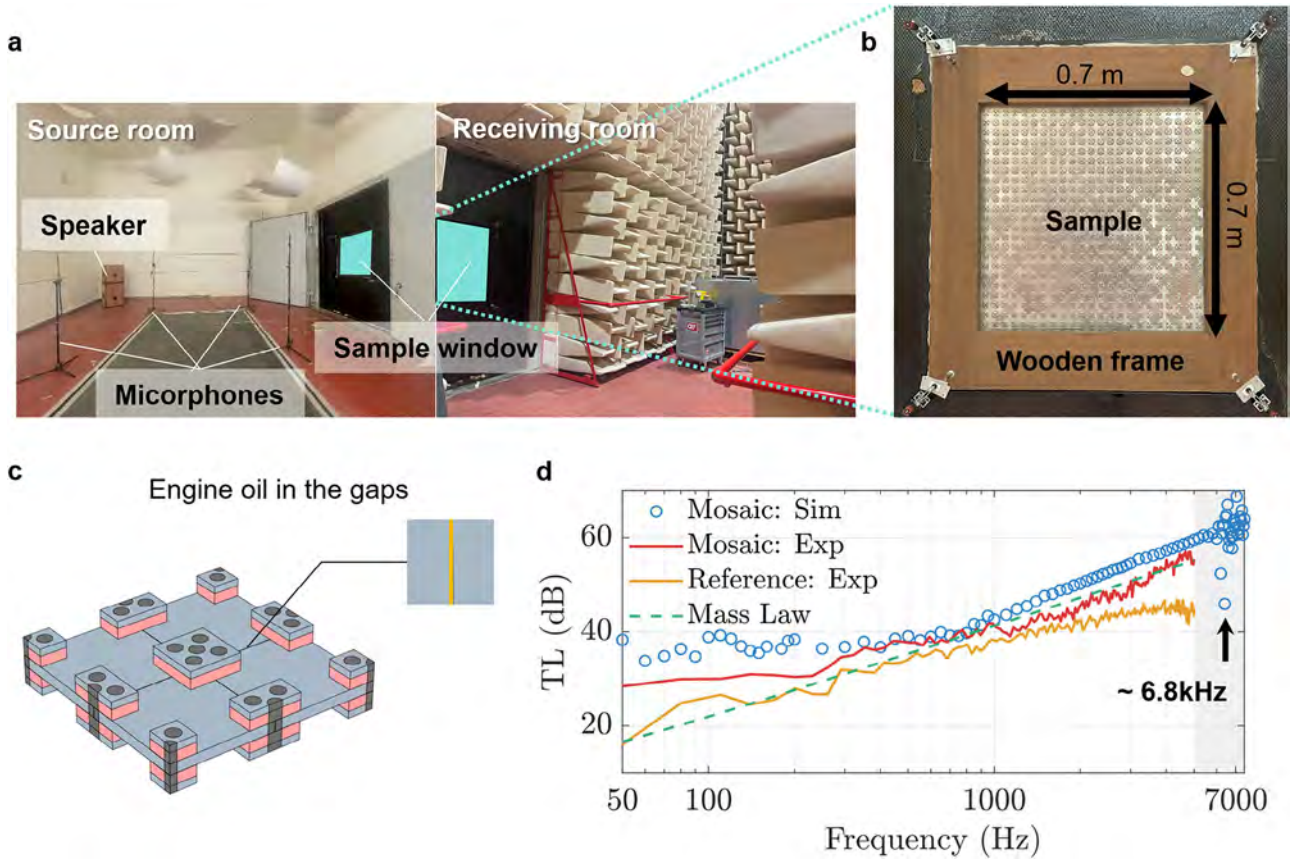

Figure 4. Acoustic transmission loss for the mosaic plate sample and the reference plate: a) Photos of the reverberation room (left) for the sound source, and the semi-anechoic room for measuring the transmission (right). The source room has two speakers placed at the corners and a microphone array in the center region. The diffuse sound captured by the microphone array placed in the center of the room is taken to be the incident sound on the sample. b) The mosaic plate sample was fixed with two wooden frames and the whole structure was clamped to the edges of the window connecting the two chambers. The size of the sample window is 0.7 m × 0.7 m. c) Engine oil (yellow region) fills the gaps of the MPt to prevent leakage of incident sound waves. d) Comparison of mass density law (green dashed line) with simulation result (hollow blue dot). Here the yellow line delineates the measured results for the reference plate, and the red line is that for the MPt. The experimental test frequency range is 50 Hz to 5 kHz, but the simulation results extend to 7.5 kHz. The experimental results are moving-window averaged over a window width of 30 Hz. For the MPt, deviation from the mass density law is clearly seen below 600 Hz.

the mass density law significantly above 1 kHz. The latter is based on normal incidence.

In Figure 4d, the mass density law and the simulation results were obtained under the normal incidence condition, whereas the experimental results on MPt and the reference plate were obtained under the diffuse incidence condition. Hence accurate comparisons should be between those with identical incidence conditions. For the simulation results, it is seen that in the low frequency regime, the MPt shows a significant advantage over the mass density law, which basically expresses the inertial effect as dictated by Newton's law. Here the damping effect of the soft layers at the corners of each TP, through the conversion of normal TP displacement to lateral displacement of the soft layers at the open boundaries, played an important role. The mosaic geometry plays the role of focusing the stress at TP's corners, thereby making the dampling effect of the soft layer especially effective. This advantage persisted even in the high frequencies. For the comparison between the experimental results on the MPt with that of the reference plate, it is observed that the measured results on MPt not only reproduced the qualitative behavior exhibited by the simulations in the low-frequency regime, but also displayed a TL advantage over the reference plate all the way to the upper end of the measured results at 5 kHz.

It should be noted that the data plotted in Figure 4d were moving-window averaged with a window width of 30 Hz. Without the moving-window averaging, there can be significant oscillations in the measured results below 100 Hz, owing to the finite size of the reverberation source room, so that the sound modes become discrete below 100 Hz. The oscillations reflect this discreteness.

Overall, the MPt provides an average of 13 dB higher sound insulation at the ultralow frequency of 50 Hz, as compared to a uniform plate of the same mass density and dimensions. The MPt also shows a noticeable higher sound insulation effect at high frequencies, demonstrating that the mosaic design can indeed deviate significantly from the mass density law over a broad frequency range.

The results show that mosaic design holds promise for practical integration into lightweight, deployable structures such as ship hulls, aerospace panels, and portable acoustic shields, where

both wave attenuation and structural rigidity are required. Beyond acoustics, it may be extended to elastic or mechanical metamaterials for vibration isolation and mechanical filtering. These features together suggest that the design could serve as a versatile platform for future multifunctional systems incorporating sensing, actuation, or energy harvesting.

3. Conclusion

In this work, we propose a mosaic plate design that can demonstrate a zero-frequency bandgap in the broadband frequency range of 0^+-6.8 kHz, as well as display effective sound insulation. The effects were verified by both simulations and experiments. In the design of the MPt, the TPs are linked at corners by screws and stabilized by the JPs. Each JP comprises two smaller-sized aluminum pieces on opposite sides of the TPt, with two silicone rubber layers sandwiched in between. The overall structure exhibits static rigidity while displaying an absence of modes at frequencies between 0^+ and the locally resonant mode at 6.8 kHz. Furthermore, the application of the MPt in sound insulation was analyzed through both simulations and experiments, showing an excellent sound insulation effect that exceeds the performance predicted by the mass density law. Our results provide valuable insights into the design and application of acoustic and mechanical metamaterials, especially in the low-frequency regime. Future work will explore how nonlinear interactions between bandgap formation and stress-driven energy transfer at geometric interfaces can unify low- and mid-frequency wave suppression within a single broadband metamaterial design.

4. Experimental Section

Simulation Setting: The commercial software COMSOL Multiphysics 6.0 was adopted for simulations. The Solid Mechanics eigenfrequency module was used for the dispersion calculation (Figure 2b), with the Floquet boundary condition applied to the boundaries of the unit cell. For the simulations involving sound transmission loss (Figure 4d), the Solid Mechanics module was combined with the Pressure Acoustics module. The former was responsible for the domain of the mosaic plate sample, whereas the latter was responsible for the air domain. For the solid-fluid interfaces at the gaps, continuity boundary conditions were applied for the displacement and stress fields. The lateral boundaries of the simulation were set to be the Floquet boundary condition. The boundaries of the TPs' gap area were defined as the "slit" in narrow region acoustics and were refined with a denser mesh. Localized free tetrahedral mesh refinements (minimum element size = 0.05 mm) were implemented near gaps and joints to resolve stress singularities. Additional information about simulation results is provided in Section S6 (Supporting Information).

Sample Fabrication and Assembly: The mosaic plate sample in the experiment consists of two sizes of aluminum alloy sheets (TP: 30 mm × 30 mm × 3 mm, JP: 15 mm × 15 mm × 2 mm), the soft layer of silicone rubber 15 mm × 15 mm × 3 mm and two specifications of screws, 4 mm and 3 mm diameters. The metal sheets were all manufactured using CNC (Computer Numerical Control) precision machining. For the TP, the four holes and the quarter holes on the corners were all threaded. For the JP Al pieces, there are two types: one is to be assembled on the top, and its central hole is threaded, while the other holes are unthreaded. For the JP Al piece to be assembled on the bottom, all the holes are unthreaded. The production of the soft layer was achieved by mixing two reagents of silicone rubber (Smooth-on Mold Max 30), pouring them into a hard mold made by 3D printing, curing for 24 hours, and demolding. The Young's modulus of the soft layer is obtained through uniaxial tensile testing using a universal testing machine. More details of the sample preparation are described in Section S1 (Supporting Information).

Experimental Setups: In the vibration test, a laser vibrometer system was used for precise measurements. Excitation was applied to the back of the sample at the input end using a shaker (The Modal Shop 2075E) connected to an amplifier (SmartAmp 2100E21-400), which served as the point source. The laser vibrometer (Polytec PSV-500) was aimed at the front of the sample to perform scanning over the scanning area. The scanning grid was centered on each TP, with a spacing of 30.1 mm between adjacent scanning points. This resulted in a total of 20 × 20 scanning points. The same scanning grid configuration was applied to the reference stainless steel plate. In the acoustic transmission loss test (ISO 15186-1), a reverberation chamber equipped with two loudspeakers and a microphone array served as the source room with diffuse incident sound waves. The receiving room is a semi-anechoic chamber. A handheld sound intensity probe (B&K Type 3599) was manually operated during the test to perform near-field scanning on the receiver side. The scanning was conducted approximately 10 cm from the sample surface, to measure the average near-field sound pressure of the sample. Further details of the vibration and acoustic tests are summarized in Section S3 and S4 (Supporting Information).

Supporting Information

Supporting Information is available from the Wiley Online Library or from the author.

Acknowledgements

N.G. thanks Sécail-Géraud Mathieu and Foucart Félix for assistance in vibration testing, Nicolas Poulain for sound insulation experiments, Meziere Herve for sample preparation and Mathieu Gaborit for the soft material performance characterization. This project has received funding from the Horizon Europe Marie Skłodowska-Curie Actions grant agreement No. 101106904 MDS-APP-UAF. P.S. acknowledges helpful discussions with John Willis. V.R.-G., J.-P.G., and P.S. thank Isaac Newton Institute for Mathematical Sciences for support and hospitality during the program "The Theory and Applications of Multiple Wave Scattering" when the initial idea of this piece took shape and coalesced. V.R.-G. is grateful for the partial support under Grant No. PID2023-146237NB-I00 funded by MICIU/AEI/10.13039/501100011033.

Conflict of Interest

The authors declare no conflict of interest.

Author Contributions

P.S. initiated the idea and supervised the research. N.G. did the simulations, carried out the sample fabrication and experimental measurements, and contributed to the initial draft. V.R.-G and J.-P.G. contributed to and supervised the theoretical aspects of this work. J.-P.G. contributed to the sample fabrication and experimental measurements. All contributed to the final draft.

Data Availability Statement

The data that support the findings of this study are available from the corresponding author upon reasonable request.

Keywords

broadband zero-frequency bandgap, locally resonant, mass law, metamaterials, vibration and sound isolation

Received: April 1, 2025
Revised: June 15, 2025
Published online:

[1] D. Royer, E. Dieulesaint, *Elastic Waves in Solids I: Free and Guided Propagation*, Springer Science & Business Media, Berlin **1999**.
[2] R. Craster, S. Guenneau, M. Kadic, M. Wegener, *Rep. Prog. Phys.* **2023**, *86*, 094501.
[3] N. Gao, J. Li, R. Bao, W. Chen, *Soft Matter* **2019**, *15*, 2921.
[4] J. Li, N. Gao, R. Bao, W. Chen, Mechanics of High-Contrast Elastic Solids: Contributions from Euromech Colloquium *626*,Springer, Berlin **2023**,
[5] Z. Liu, X. Zhang, Y. Mao, Y. Y. Zhu, Z. Yang, C. T. Chan, P. Sheng, *Science* **2000**, *289*, 1734.
[6] G. Ma, C. Fu, G. Wang, P. Del Hougne, J. Christensen, Y. Lai, P. Sheng, *Nat. Commun.* **2016**, *7*, 13536.
[7] G. Ma, P. Sheng, *Sci. Adv.* **2016**, *2*, 1501595.
[8] Y.-F. Wang, Y.-Z. Wang, B. Wu, W. Chen, Y.-S. Wang, *Appl. Mech. Rev.* **2020**, *72*, 040801.
[9] A. Colombi, P. Roux, S. Guenneau, P. Gueguen, R. V. Craster, *Sci. Rep.* **2016**, *6*, 19238.
[10] D. Colquitt, A. Colombi, R. Craster, P. Roux, S. Guenneau, *J. Mech. Phys. Solids* **2017**, *99*, 379.
[11] A. Colombi, D. Colquitt, P. Roux, S. Guenneau, R. V. Craster, *Sci. Rep.* **2016**, *6*, 27717.
[12] Y. Lai, Y. Wu, P. Sheng, Z.-Q. Zhang, *Nat. Mater.* **2011**, *10*, 620.
[13] S. Yao, X. Zhou, G. Hu, *New J. Phys.* **2010**, *12*, 103025.
[14] M. I. Hussein, M. J. Leamy, M. Ruzzene, *Appl. Mech. Rev.* **2014**, *66*, 040802.
[15] C. Poulton, A. Movchan, N. Movchan, R. C. McPhedran, *Proc. R. Soc. A* **2012**, *468*, 1196.
[16] Y. Achaoui, T. Antonakakis, S. Brûlé, R. Craster, S. Enoch, S. Guenneau, *New J. Phys.* **2017**, *19*, 063022.
[17] M. H. Bae, W. Choi, J. M. Ha, M. Kim, H. M. Seung, *Sci. Rep.* **2022**, *12*, 3993.
[18] Z. Chen, G. Wang, W. Zhou, C. Lim, *Int. J. Mech. Sci.* **2021**, *194*, 106215.
[19] Q. Zhang, D. Guo, G. Hu, *Adv. Funct. Mater.* **2021**, *31*, 2101428.
[20] Q. Lin, J. Zhou, K. Wang, D. Xu, G. Wen, Q. Wang, *Compos. Struct.* **2023**, *307*, 116656.
[21] J. Zhou, K. Wang, D. Xu, H. Ouyang, *J. Appl. Phys.* **2017**, 121.
[22] J. Zhou, H. Pan, C. Cai, D. Xu, *Int. J. Mech. Mater. Des.* **2021**, *17*, 285.
[23] Y. Zeng, L. Cao, S. Wan, T. Guo, S. An, Y.-F. Wang, Q.-J. Du, B. Vincent, Y.-S. Wang, B. Assouar, *Appl. Phys. Lett.* **2022**, *121*.
[24] C. Yilmaz, G. M. Hulbert, N. Kikuchi, *Phys. Rev. B—Condens. Matter Mater. Phys.* **2007**, *76*, 054309.
[25] N. M. Frandsen, O. R. Bilal, J. S. Jensen, M. I. Hussein, *J. Appl. Phys.* **2016**, *119*.
[26] M. H. Bae, J. H. Oh, *Mech. Syst. Signal Process.* **2022**, *170*, 108832.
[27] P. Wang, J. Shim, K. Bertoldi, *Phys. Rev. B—Condens. Matter Mater. Phys.* **2013**, *88*, 014304.
[28] H. Ding, L.-Q. Chen, *Nonlinear Dyn.* **2019**, *95*, 2367.
[29] A. Álvarez-Trejo, E. Cuan-Urquizo, D. Bhate, A. Roman-Flores, *Mater. Des.* **2023**, *233*, 112190.
[30] A. Nateghi, L. Van Belle, C. Claeys, E. Deckers, B. Pluymers, W. Desmet, *Int. J. Mech. Sci.* **2017**, *127*, 73.
[31] S. Wang, Z. Wang, *Mech. Syst. Signal Process.* **2022**, *181*, 109489.
[32] Y.-Z. Wang, L. Ma, *J. Vib. Control* **2024**, *30*, 2993.
[33] X. Xu, M. V. Barnhart, X. Li, Y. Chen, G. Huang, *J. Sound Vib.* **2019**, *442*, 237.
[34] M. Miniaci, A. Krushynska, A. S. Gliozzi, N. Kherraz, F. Bosia, N. M. Pugno, *Phys. Rev. Appl.* **2018**, *10*, 024012.
[35] C. Mei, L. Li, H. Tang, X. Han, X. Wang, Y. Hu, *Compos. Struct.* **2021**, *271*, 114118.
[36] A. Arjunan, A. Baroutaji, J. Robinson, A. Vance, A. Arafat, *Build. Environ.* **2024**, *251*, 111250.
[37] A. Arjunan, C. Wang, M. English, M. Stanford, P. Lister, *Metals* **2015**, *5*, 1414.
[38] P. Sheng, *Introduction to Wave Scattering, Localization, and Mesoscopic Phenomena*, Springer, Berlin **1996**.
[39] D. T. Blackstock, *Fundamentals of Physical Acoustics*, John Wiley & Sons, New York **2000**.

